minerals

Article

Early Diagenesis in the Lacustrine Ostracods from the Songliao Basin 91.35 Million Years Ago and Its Geological Implications

Zhenwu Liu [1,2], Yuke Liu [2], Xuejia Du [3], Dan Lyu [1], Huaichun Wu [1,*] and Huajian Wang [2,*]

[1] School of Ocean Sciences, China University of Geosciences (Beijing), Beijing 100083, China
[2] Research Institute of Petroleum Exploration and Development, Beijing 100083, China
[3] Department of Petroleum Engineering, University of Houston, Houston, TX 77023, USA
* Correspondence: wanghuajian@petrochina.com.cn (H.W.); whcgeo@cugb.edu.cn (H.W.); Tel.: +86-010-8359-5538 (Huajian Wang)

Abstract: Diagenesis is a double-edged sword of geochemical recordings. It makes us always doubt about the representativeness of many geochemical indicators, especially the isotope and mineral related. It also provides a window to explore the biogeochemical processes at the water–rock interface, which are related to the interactions between the hydrosphere, biosphere, and lithosphere. In this study, we identified microbial early diagenesis in lacustrine ostracods from the Songliao Basin 91.35 million years ago by using in situ mineralogical and carbon isotope analytical methods. Our results suggest multiple biological early-diagenesis processes and the formation of a ferric and methane transition zone (FMTZ) in the sulfate-poor pore water, which are conducive to the formation of dolomite and ankerite. These secondary carbonate minerals related to dissimilatory iron reduction and methanogenesis have heavier carbon isotopic compositions than the calcified ostracod shell in the water column and might bring interferences to the geochemical parameters of ostracods.

Keywords: ankerite; carbon isotope; dissimilatory iron reduction; dissolved inorganic carbon; early diagenesis; ferric and methane transition zone; methanogenesis; ostracod

check for updates

Citation: Liu, Z.; Liu, Y.; Du, X.; Lyu, D.; Wu, H.; Wang, H. Early Diagenesis in the Lacustrine Ostracods from the Songliao Basin 91.35 Million Years Ago and Its Geological Implications. *Minerals* **2023**, *13*, 5. https://doi.org/10.3390/min13010005

Academic Editors: Hamzeh Mehrabi and Vahid Tavakoli

Received: 13 November 2022
Revised: 14 December 2022
Accepted: 15 December 2022
Published: 20 December 2022

1. Introduction

Reconstruction of the water conditions of paleo-oceans and -lakes is of great importance in understanding the living environment of ancient life. Due to the ubiquitous diagenesis, many important geochemical parameters obtained from whole rock analysis, such as inorganic carbon and oxygen isotopes of carbonate ($\delta^{13}C_{carb}$ and $\delta^{18}O_{carb}$), strontium isotope ($^{87}Sr/^{86}Sr$), anomalies of rare earth elements (REE), etc., need to be carefully used [1–3]. The emergence and evolution of shelled organisms since the terminal of the Neoproterozoic Era [4], provide an effective archive for the primary geochemical information of the paleo-waters in their skeletonized shells. Geochemical compositions of some calcified zooplankton shells, such as foraminifera and ostracoda, are widely used in the reconstruction of paleo-climatic, -oceanographic and -ecological changes [5,6].

Carbon isotope of calcified zooplankton shells ($\delta^{13}C_{carb}$) is one of the most representative proxies to reveal the environments of paleo- oceans and -lakes, as well as the atmospheric carbon dioxide (CO_2) concentration [7–9]. Long-time scale and high-precision $\delta^{13}C_{carb}$ data play an important role in the stratigraphic correlation, paleoenvironment reconstruction, and deep-time carbon cycle modeling. For example, due to the $\delta^{13}C_{carb}$ of benthic foraminiferal and the micro-plankton criteria, the Abiod Formation of north-central Tunisia is restricted to the Late Campanian age, and the Campanian/Maastrichtian boundary is placed within the lowermost part of the El Haria Formation [10]. A high-resolution, benthic foraminiferal $\delta^{13}C_{carb}$ curve from the northwest Pacific ODP Site 1209 spanning 44 to 56 million years ago (Ma) with five thousand years (kyr) resolution, presents several excursions corresponding in timing and magnitude to hyperthermal layers previously described elsewhere [11].

Ostracods are one class of the oldest known microfauna, containing both marine and non-marine forms [12]. The first fossil representatives are from marine sediments 485 Ma [13] and have molecular clock evidence 600 Ma or earlier [14]. The earliest freshwater ostracoda species came from coal-forming swamps, ponds, and streams of the Pennsylvanian age (318~299 Ma) [15]. Preservation of ostracod fossil is attributed to the calcified shell present in most species, which is a valuable source of calcite. Carbon isotope analyses of ostracod shells have concentrated on lacustrine environments, from which other carbonate microfossils are largely absent [5]. The specimens' $\delta^{13}C_{carb}$ values are mainly controlled by the calcification completion of shell, the equilibrium with dissolved inorganic carbon (DIC) in the water column and pore water, as well as the seasonal and vertical variations of the carbon isotopic compositions of DIC ($\delta^{13}C_{DIC}$) [16]. In most cases, the impact of the first two factors is assumed to be negligible or in equilibrium. Then, the variation of ostracods' $\delta^{13}C_{carb}$ values were used to represent the climate and biological activities forced changes of $\delta^{13}C_{DIC}$. For example, the ostracods' $\delta^{13}C_{cal}$ values of the Late Cretaceous sediments from the Songke1s and Songke1n cores in the Songliao Basin, were considered to reflect changes in both global climate and regional basin evolution [17].

However, during the burial and early diagenetic stage, a series of heterotrophic microbial processes occurs to degrade organic matters and generate secondary carbonate minerals, such as dolomite, calcite, ankerite, and siderite [18–21]. As the bicarbonate (HCO_3^-) forming these secondary minerals is mainly from pore water rather than water column [19,22], the minerals are encased in ostracod shells and may be difficult to effectively remove, thereby causing geochemical contamination. Therefore, it is necessary to identify and evaluate the early diagenesis in the ostracods.

In this study, in situ mineralogical and carbon isotopic analyses of lacustrine ostracods from the Songliao Basin were performed by using quantitative evaluation of minerals by scanning electron microscopy (QemScan) and laser ablation isotope ratio mass spectrometry (LA-IRMS), respectively. Abundant ankerite, chlorite, and scarce pyrite in the studied ostracods indicated the occurrence of early diagenesis and the formation of a ferric-methane transition zone which generated ^{13}C-enriched ankerite. Our results support more strict treatment and in situ high-precision analysis to improve the reliability of ostracod-based geochemical data.

2. Sample Preparation and Analytical Methods

2.1. Sample Preparation

The ostracod samples are from Songke1s core with a depth of 1734 m in the Songliao Basin, northeast of China (Figure 1a). Three high-precision CA-ID-TIMS U–Pb zircon ages of 91.886 ± 0.11 Ma, 90.974 ± 0.12 Ma and 90.536 ± 0.12 Ma from the bentonites at 1780 m, 1705 m and 1673 m of the Songke1s core [23] and the critical astrochronological time scale [24,25] together constrain the samples' age to be 91.35 Ma (Figure 1b). The Songliao Basin is a large lacustrine basin filled with the Mesozoic and Cenozoic sediments [26]. Two sets of organic-rich black shales, Qingshankou and Nenjiang formations, mostly developed in the deep-water phases and became the main source rocks of the Songliao Basin [27]. The salinity of paleo-Songliao lake is interpreted as predominantly freshwater to oligohaline with multiple and small-scale seawater incursion events [28]. Although fourteen non-marine ostracod assemblage zones have been identified from the Member 1 of the Qingshankou Formation (K_2qn^1) to the Member 2 of the Nenjiang Formation (K_2n^2), only one assemblage zone coincides in the K_2qn^1 and is dominated by *Triangulicypris torsuosus* Netchaeva with a smooth shell and *Triangulicypris torsuosus* Netchaeva. *nota* Ten with tubercles [29]. These ostracods are rare in the black shales but are enriched in several individual layers. The studied samples are handpicked from the middle of K_2qn^1, with a lithological characteristic of centimeter-thick ostracod layers interbedded with micrometer-thick organic-rich laminae (Figure 1c).

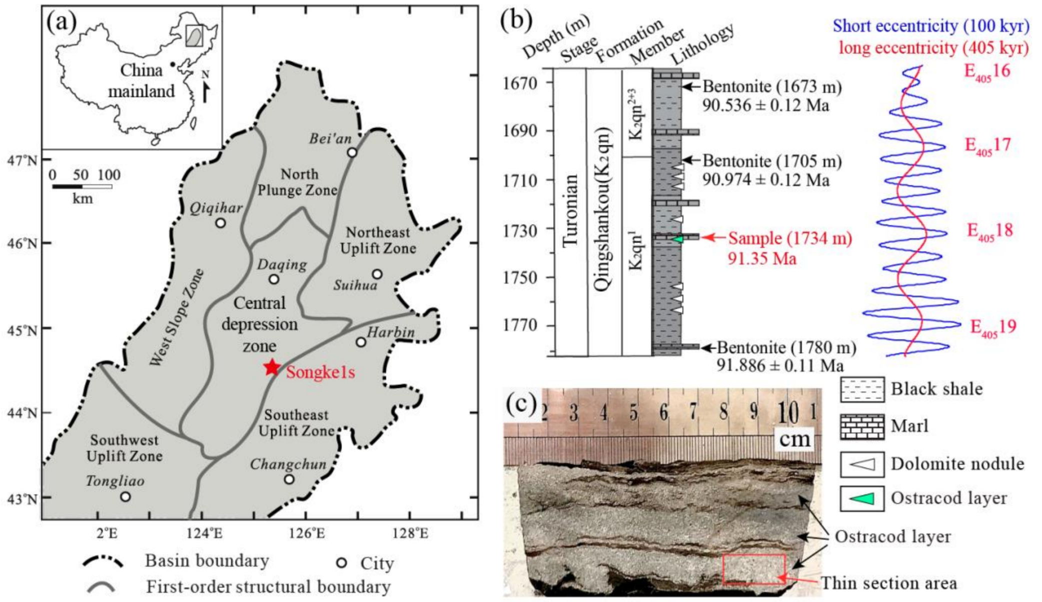

Figure 1. (**a**) Location of the Songke1s core in the Songliao Basin, northeast of China. (**b**) Stratigraphy, geochronology, and astrochronology of the Songke1s core in the 1782–1667 m range. The sample age (91.35 Ma) in this study was calculated from the high-precision U-Pb zircon ages [23] and the critical astronomical time scale tune by short eccentricity [24,25]. (**c**) Hand specimen characteristic of the studied ostracod layer. Thin sections were prepared from the area without organic-rich lamina.

Several standard thin sections with a 1.5 cm × 3 cm area were prepared. The thickness of lamina used for optical observation and LA-IRMS analysis was 30 μm and 200 μm, respectively, as the latter one met the requirement to provide sufficient laser ablated samples from micro-areas (at least 150-μm-thickness). Carbon-coated fragments with new fractures were prepared for scanning electron microscope (SEM) observation. Carbon-coated fragments with argon ion polished surface were prepared for QemScan analyses. These sections and fragments are from the same depth range to ensure the data comparability between different analyses (Figure 1c).

2.2. Optical Observation and Mineralogical Analyses

Optical observation of ostracods on sections was investigated by using optical microscope (Olympus 4500P, Olympus Company, Tokyo, Japan) under transmission light at the key laboratory of petroleum geochemistry of China National Petroleum Corporation (CNPC, Beijing, China), Research Institute of Petroleum Exploration and Development (RIPED). The carbon-coated fragments were examined by using a Apreo SEM (FEI Company, Hillsboro, OR, USA) equipped with an energy dispersive X-ray spectroscopy (EDS) for the semi quantitative element determination. An integrated high-speed detector (Bruker Company, Billerica, MA, USA) was used for backscattered electron (BSE) image and secondary electron image (SEI). The beam accelerating voltage was 15 kV, and the emission current was 71 mA.

Elemental imaging and mineral identification were performed at the key laboratory of hydrocarbon reservoir of CNPC, RIPED, by using a QemScan 650F (FEI Company, Hillsboro, OR, USA) with a pixel size of 1 μm. This instrument emits an X-ray spectrum and provides information on the content of elements at each measured point. The elemental contents were obtained by combining the BSE, image gray, and X-ray intensity, and then were converted into mineral phases. Individual mineral was identified by referring to a comprehensive mineral database incorporated into the QemScan software iExplorer. Several important elements, including aluminum (Al), calcium (Ca), iron (Fe), magnesium (Mg), silicon (Si), and sulfur (S) were selected for in situ imaging.

2.3. Laser Ablation Isotope Ratio Mass Spectrometry Analysis

In situ carbon isotope analysis was carried out in the key laboratory of carbonate reservoir of CNPC, RIPED. This experiment was performed on a coupled system of a Nd-1064 Nd:YAG laser ablation (Norla Institute of Technical Physics, Chengdu, Sichuan, China), a self-assembled elemental analyzer, and an isotope ratio mass spectrometer (Thermo, DELTA V Advantage, Waltham, MA, USA) (Figure 2). This system contains a movable sample stage that can be monitored by a computer-controlled video microscope (20 to 80×) and an internal light-emitting diode (LED) illumination. Due to the small amount of solid gas produced by laser ablation, the sample amount generated by a single ablation cannot generate sufficient CO_2 for mass spectrometry analysis. Therefore, we added a cold trap between LA and IRMS to capture and enrich the gas generated by multiple ablations (Figure 2). All laser carbonate systems to isotope operate on the principle of thermal decrepitation during laser heating by the following reaction (Equation (1)) [30].

$$M^{2+}CO_3 \rightarrow M^{2+}O + CO_2 \quad (1)$$

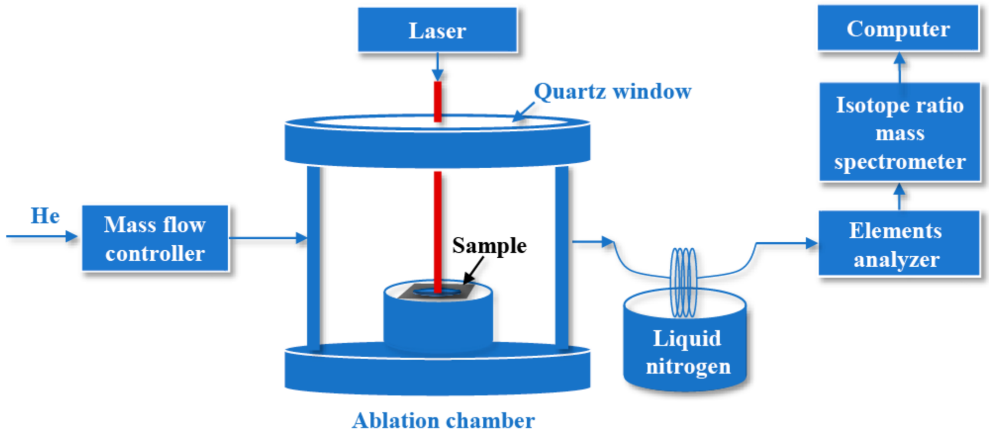

Figure 2. Diagram of the laser ablation isotope ratio mass spectrometry analysis.

After laser ablation, the generated CO_2 was frozen on a 0.5 mm i.d. fused silica capillary immersed in a liquid nitrogen bath. The trapping began a few seconds before ablation and continued for a total of 60 s. In most cases, the trapping continued for at least 30 s after sample ablation. Following the trapping step, we switched the carrier gas flow through the trap, reducing the high flow rate (10 mL/min) to a low flow rate (1 mL/min). Once the carrier gas flow rate was low enough, the capillary from the liquid nitrogen bath was removed. The CO_2 rapidly melted at room temperature and was transferred by the carrier gas to pass through a column in the element analyzer, which was filled with magnesium perchlorate ($Mg(ClO_4)_2$) to remove the organic matter and water and then passed through a quartz capillary to separate other possible debris.

Following the element analyzer, the CO_2 pulse passed into the IRMS instrument via an open split. The duration for each analysis, from ablation to isotope analysis, was about 8 min. High purity helium (with a volume fraction over 99.999%) was used as carrier gas to reduce potential CO_2 contamination from the atmosphere and improve transmission efficiency. For blank runs following the same method without any laser ablation, the CO_2 peaks were too small to be noticed for sample analysis. The national standard material GBW04405 with a uniform $\delta^{13}C$ value of 0.57 ± 0.03‰ was selected as the standard sample to optimize the operating parameters. With the selected and optimized operating conditions (Table 1), we can obtain stable $\delta^{13}C$ values of the standard samples with an uncertainty lower than ±0.2‰ (1σ) over 10 times tests. All $\delta^{13}C$ values were reported relative to the Vienna Pee Dee Belemnite (VPDB), with standard deviation (SD) of each sample being lower than ±0.2‰ based on three times analyses.

Table 1. Measurement parameters of LA-IRMS.

Laser Ablation System (LA)		Isotope Ratio Mass Spectrometry (IRMS)	
Wavelength	1064 nm	High voltage	3.0 KV
Pulse frequency	10 Hz	Box emission	0.8 mA
Pulse energy	66 μJ	Trap emission	0.7 mA
Output of energy	50%	Carrier gas (He)	1–10 mL/min
Energy density	7 J/cm^2	Data acquisition	Thermo Isodat 3.0
Spot size	50 μm	Temperature	26 °C
Scanning mode	Point	Humidity	52% RH
Pause time	1 s	Elemental isotope	^{13}C

3. Results

3.1. Petrographic and Mineralogical Features

The ostracod layer is mainly composed of ostracod shells, detrital quartz, and clay minerals. Most ostracods are well preserved in oval features with 0.7–1.2 mm for the long axis and 0.3–0.8 mm for the short axis (Figure 3). Their body sizes are similar to the previously reported *Triangulicypris torsuosus* Netchaeva and *Triangulicypris torsuosus* Netchaeva. *nota* Ten occurred in the K_2qn^1 [29]. As shown in Figure 3, most ostracods are filled with carbonate minerals and/or clay minerals, accounting for about half-and-half in observed area.

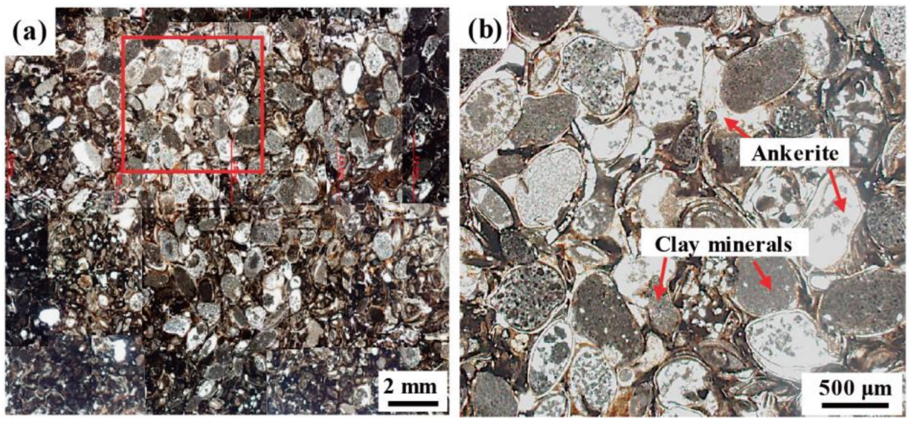

Figure 3. Petrographic features of the studied ostracod layer under transmission light. (**b**) is the enlargement of marked square area in (**a**). The white and gray fillings in the ostracods under transmission light are ankerite and clay minerals, respectively.

The well-preserved ostracods cluster together more clearly under SEM (Figure 4a). Both *Triangulicypris torsuosus* Netchaeva and *Triangulicypris torsuosus* Netchaeva. *nota* Ten are identified and presented in Figure 4b,c. The EDS data showed that the ostracod shell is composed of highly purified calcite ($CaCO_3$) with a sum atomic percentage of calcium (Ca), carbon (C), and oxygen (O) over 97% (Figure 4c, Table 2). The randomly oriented clay mineral with high atomic percentages of Fe (7.9%), Al (6.1%), Si (6.9%), and Mg (3.5%) (Figure 4d, Table 2) may be chlorite [$Y_3[Z_4O_{10}](OH)_2 \cdot Y_3(OH)_6$, Y = Fe, Al, Mg; Z = Si, Al]. The C-axis of this mineral can take any rotation angle on surface (Figure 4d). The rhombohedron of euhedral-subhedral shape carbonate mineral with a diameter of several to tens of micrometers and a higher atomic percentage of Fe (6.7%) than Mg (5.5%) (Figure 4e,f, Table 2) may be ankerite [$Ca(Mg_x, Fe_y)(CO_3)_2$, $x < y$]. Ankerite with a similar occurrence also can be found in the ostracod filled with chlorite (Figure 4d), further indicating the extensive distribution of ankerite.

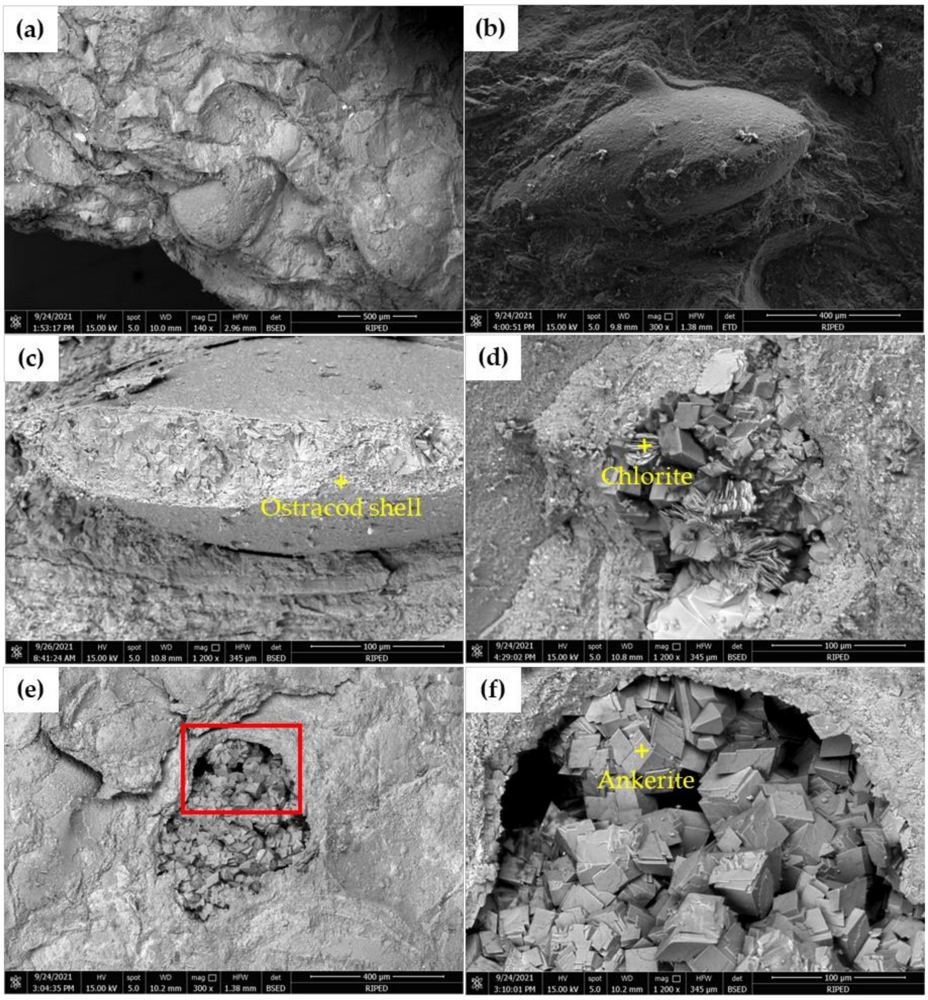

Figure 4. Scanning electron microscope photographs of the studied ostracods. (**a**,**b**) are appearances of well-preserved ostracod shells. (**b**) is *Triangulicypris torsuosus* Netchaeva. *nota* Ten with a tubercle. (**c**) is *Triangulicypris torsuosus* Netchaeva with a smooth shell. (**d**) is a broken ostracod filled with chlorite and ankerite. (**e**) is a broken ostracod filled with ankerite. (**f**) is the enlargement of marked area in (**e**). Energy dispersive X-ray spectroscopy (EDS) analysis was performed on the points with yellow cross forks in panels (**c**,**d**,**f**). The EDS data are shown in Table 2.

Table 2. Elemental contents of different points on sample based on SEM-EDS method.

Points	Units	Al	C	Ca	Fe	Mg	O	S	Si
Calcified ostracod shell (Figure 4c)	Un-normalized count (wt%)	0.5	8.0	24	0.8	0.4	26	0	0.7
	Normalized count (wt%)	0.9	13.2	39	1.3	0.7	43	0	1.2
	Atomic count (at%)	0.7	22.4	20	0.5	0.6	55	0	0.9
Chlorite (Figure 4d)	Un-normalized count (wt%)	7.3	5.2	6.0	17	3.3	37	0.1	8.2
	Normalized count (wt%)	8.7	6.2	7.1	20	4.0	44	0.1	9.7
	Atomic count (at%)	6.1	11.1	3.8	7.9	3.5	59	0.1	6.9
Ankerite (Figure 4f)	Un-normalized count (wt%)	0.4	5.1	24	11	3.8	23	0	0.3
	Normalized count (wt%)	0.6	7.6	35	16	5.7	35	0.1	0.5
	Atomic count (at%)	0.5	14.9	21	6.7	5.5	51	0	0.4

Elemental and mineralogical distributions of two types of ostracods filled with chlorite and ankerite were further investigated by using QemScan. Both of them show concentric mineralogical distribution inside (Figures 5 and 6). The co-enrichment of Fe, Ca, and Mg represents ankerite. The co-enrichment of Al, Si, Mg, and Fe is consistent with chlorite. Pyrite (FeS_2) is characterized by the co-enrichment of Fe and S. Quartz (SiO_2) is characterized by extreme enrichment of Si. The QemScan data give more refined mineral distributions and are consistent with the optical observation (Figures 3 and 4). For the ostracod filled with ankerite, the chlorite inside is mainly adjacent to the shell (Figure 5). Conversely, when the ostracod is filled with chlorite, ankerite is the dominating secondary mineral and distributes along the shell edge (Figure 6). A small amount of siderite was also identified in this type of ostracod (Figure 6). Small amounts quartz with poor roundness can be identified on the calcified shells (Figures 5 and 6). It should be noted that pyrite is rare in both two types of ostracods and is mainly associated with ankerite (Figures 5 and 6).

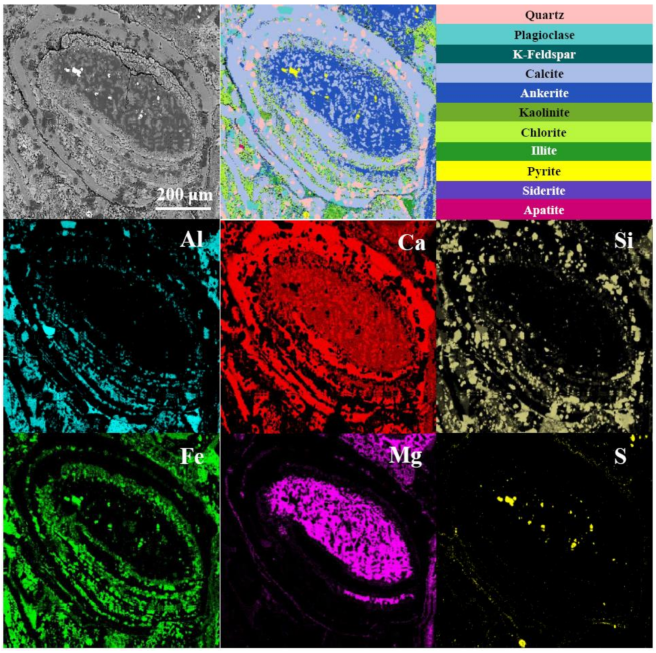

Figure 5. Scanning electron microscope photo and QemScan images of an ostracod filled with ankerite. Color brightness in each map represents relative abundance of its corresponding element. Brighter color indicates higher element content.

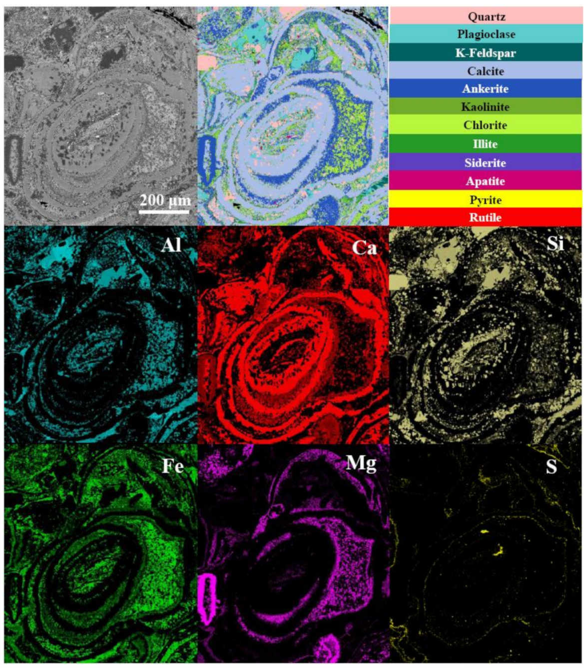

Figure 6. Scanning electron microscope photo and QemScan images of an ostracod filled with chlorite and ankerite. Color brightness in each map represents relative abundance of its corresponding element. Brighter color indicates higher element content.

3.2. Carbon Isotopic Compisitions

In situ $\delta^{13}C$ analyses of these two types of ostracods were performed on calcified shells and filling ankerites. The $\delta^{13}C$ values of calcified shells are from 0.8‰ to 1.1‰, with a mean value of 0.9‰ (Figure 7). For the ostracods filled with ankerite, the $\delta^{13}C$ values of ankerites are from 4.0‰ to 4.5‰, with a mean value of 4.2‰ (Figure 7a,b). However, low abundance of ankerite and interference from chlorite make it difficult to obtain authentic $\delta^{13}C$ values from a single ablation point. Thus, we used the liquid nitrogen freezing method to collect samples from three or four ablation points to obtain a mixed $\delta^{13}C$ value. The $\delta^{13}C$ values of ankerite in this type ostracods are from 1.9‰ to 3.0‰, with a mean value of 2.3‰ (Figure 7c,d).

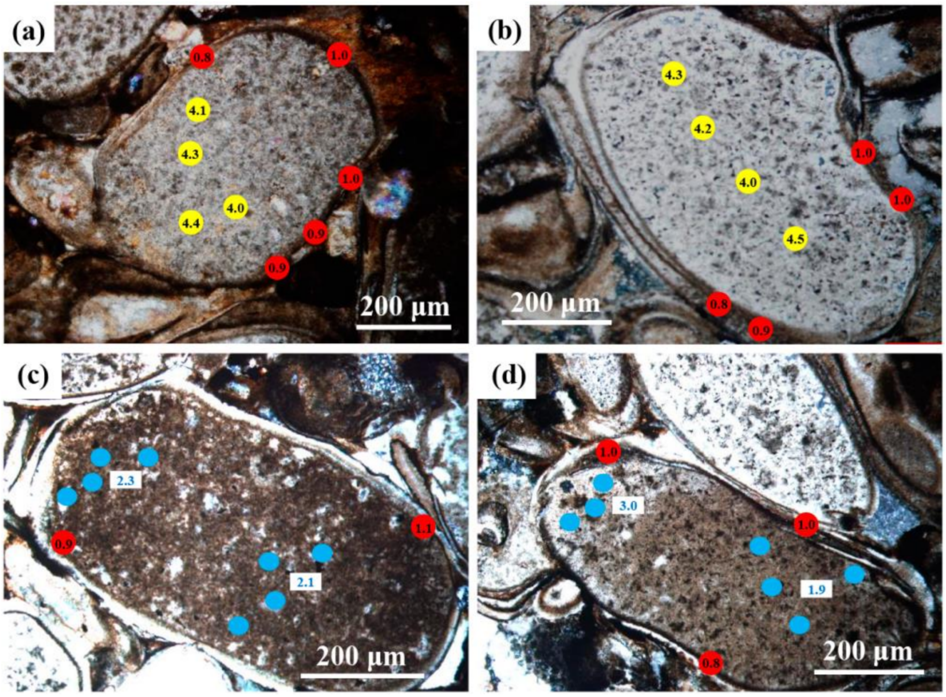

Figure 7. In situ $\delta^{13}C$ values of calcified shells and filling ankerites determined by using LA-IRMS. (**a**,**b**) are the ostracods filled with ankerite. (**c**,**d**) are the ostracods filled with chlorite. The red, yellow, and blue dots are ablation points in the experiment. Data in red and yellow dots are $\delta^{13}C$ values of calcified shells and ankerites, respectively. Data beside the blue dots are mixed $\delta^{13}C$ values of ankerite from neighbor ablation points.

4. Discussions

4.1. Microbial Early Diagenesis in the Ostracods

Three types of depositional pattern of ostracod-bearing beds have been recognized from the Songliao Basin, including mixed siliciclastic–ostracod deposits in the delta front, sheeted ostracod deposits, and dotted ostracod deposits in shallow or semi-deep lacustrine settings [31]. Here, our concerned sheeted ostracod layers with interbedded black organic-rich shales were deposited in a semi-deep lacustrine setting and were from the cementation and diagenesis of ostracods and detritus. A variety of authigenic minerals (e.g., ankerite, chlorite, pyrite, siderite) were identified in the ostracods, demonstrating complex early diagenesis during the burial of ostracods. Formation of these secondary minerals needs a relatively closed environment, which can be easily satisfied in pore water during burial time. The most important is the supply of required anions and cations, including the ferrous ion (Fe^{2+}) and hydrogen sulfide (H_2S) that are related with the water redox condition [32] and ammonia (NH_4^+) and HCO_3^- that are related with the water alkalinity [33]. The two most abundant authigenic minerals in our studied ostracods are ankerite and chlorite, both of which contain high proportion of Fe^{2+}. Previous studies showed that the comparatively large (>8 μm) and wide size distribution (8–30 μm) of the framboid diameter between 1725 and 1750 m of the Songke1s core, indicating a weakly oxic to anoxic depositional water environment [34]. Enrichments of the redox-sensitive elements supported the anoxic and non-euxinic deep water with low sulfate concentration [35]. Although Fe^{2+} is soluble in the anoxic water, it is difficult to form ankerite directly for the large enthalpies of hydration of Mg^{2+} and Ca^{2+} [36]. Transfer of Fe from water to sediment and pore water mainly depends on biotic and/or abiotic oxidation to $Fe(OH)_3$ or iron-manganese oxides, then reduced to Fe^{2+} through dissimilatory iron reduction (DIR) accompanied with the oxidation of organic matters (Equation (2), Figure 8a) [37]. This reaction will generate HCO_3^- (Equation (2), Figure 8b), which can elevate the alkalinity of pore water and is more conducive to the formation of siderite. However, the dominating carbonate mineral in our studied ostracods is ankerite rather than siderite, indicating non-dominant Fe^{2+} concentration and breakthrough of the kinetic and thermodynamic barriers of Mg^{2+} and Ca^{2+}. Experiments and geological evidence have proved that microbial mediation can realize the formation of dolomite in a low-temperature environment [38–40]. Thus, the ankerite might be from the isomorphic replacement of Mg^{2+} by Fe^{2+} in pore water [41].

$$4Fe(OH)_3 + CH_2O + 7H^+ \rightarrow Fe^{2+} + HCO_3^- + 10H_2O \tag{2}$$

The association of pyrite (even in low abundance) and ankerite proves the occurrence of bacterial sulfate reduction (BSR) and generation of H_2S (Equation (3)), which is prone to combine with Fe^{2+} to produce iron monosulfide phases (amorphous FeS) [42]. The latter will be further oxidized to pyrite (FeS_2) by elemental sulfur or other oxidants [42]. Low abundance of pyrite indicates limited sulfate supply and a narrow sulfate reduction window without free H_2S (Figure 8a) and is consistent with the previous study [35]. Bicarbonate generated through DIR and BSR processes has light $\delta^{13}C$ values (Figure 8c) for its organic origin (Equations (2) and (3)). This will produce ^{13}C-depleted carbonate minerals, e.g., the siderite with $\delta^{13}C$ values ranged from −27‰ to −8‰ from the Mesoproterozoic Xiamaling Formation [22,43] and the dolomite with $\delta^{13}C$ values lower than −10‰ from the Ediacaran Shuram Formation [1].

$$SO_4^{2-} + 2CH_2O \rightarrow H_2S + 2HCO_3^- \tag{3}$$

However, the $\delta^{13}C$ values of our studied secondary ankerites are from 1.9‰ to 4.5‰, heavier than those of the calcified shells (from 0.8‰ to 1.1‰, mean value 0.9‰). Furthermore, carbon in the ostracod shells is from the bicarbonate captured in the surface water, which usually has a heavier $\delta^{13}C$ value than that of the bottom and pore water. This can be proved by the difference of over −2‰ between the carbonate rocks deposited in deep-water and shallow facies in the same basin [44]. Variation of the $\delta^{13}C$ values of ostracods (from −6.4‰ to 4.4‰) from K_2qn^1 to the Mingshui Formation in the Songliao Basin were interpreted as the joint influence of both local basin evolution and global carbon cycle [17]. This process is mainly realized through the production and degradation of organic matter. Therefore, these seemingly contradictory measured data indicate that organic matter should have experienced further diagenetic degradation to generate ^{13}C-enriched HCO_3^-.

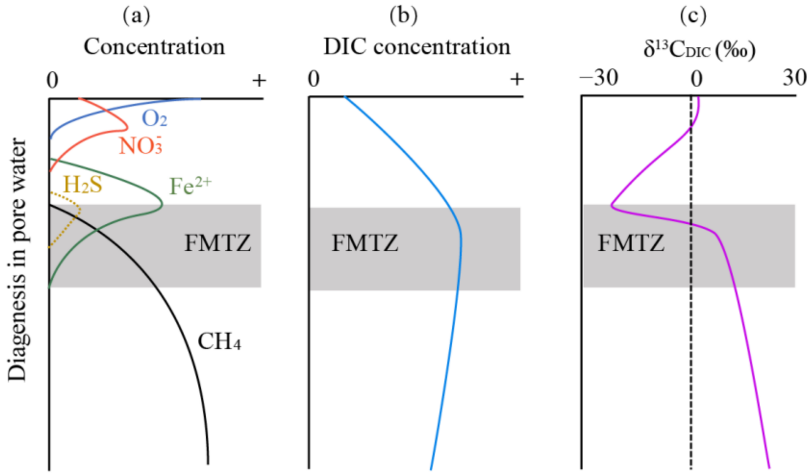

Figure 8. Schematic model of the early-diagenesis (**a**) and ferric-methane transition zone (FMTZ) controlled concentrations of dissolved inorganic carbon ((**b**), DIC) and carbon isotopic composition of DIC ((**c**), $\delta^{13}C_{DIC}$) in the pore water. Oxygen (O_2) and nitrate (NO_3^-) curves in (**a**) represent the aerobic respiration and nitrate reduction before dissimilatory iron reduction [45]. The dotted line of hydrogen sulfide (H_2S) represents that free H_2S might not exist in a sulfate-poor environment but be quickly combined with Fe^{2+} to form sulfide. The FMTZ occurs due to a lack of sulfate in pore water which impairs the sulfate reduction reaction and thus does not inhibit methanogenesis. The ^{13}C-enriched CO_2 generated through methanogenesis significantly increases the $\delta^{13}C_{DIC}$ value in the pore water (**c**) and makes an alkaline environment conducive to dolomite/ankerite precipitation and then decreases the DIC's concentration in the pore water (**b**).

Methanogenesis is the most possible process when explaining this finding (Figure 8), due to the synchronously produced extreme ^{13}C-depleted methane (CH_4, lower than −60‰) [46]. Furthermore, the mole ratio of CH_4: CO_2 is 4:1 when dissimilated for every mole C assimilated into biomass (Equation (4)) [46]. According to the isotope mass balance, if we assume the carbon isotopic value of organic matter ($\delta^{13}C_{org}$) to be −30‰ [35] and the mole ratio of methanogenic genetic HCO_3^- to pore water HCO_3^- (with an assumed $\delta^{13}C$ value of −8‰) to be higher than 1:5, it is entirely possible to generate HCO_3^- with a $\delta^{13}C$ value heavier than 8.3‰. This will cause a significant turning point of carbon isotopic composition of DIC, with a $\delta^{13}C_{DIC}$ value of pore water heavier than that of the bottom water (Figure 8c). Huge generation of HCO_3^- is also conducive to the formation of dolomite, which may result in the DIC concentration decrease after reaching supersaturation (Figure 8b).

$$5CH_2O + 6H_2 \rightarrow 4CH_4 + CO_2 + 3H_2O \quad (4)$$

In the Junggar Basin, the maximum $\delta^{13}C$ value of methanogenic genetic dolomite in the Permian Lucaogou Formation can reach 20‰ [18]. In the Ordos Basin, the carbonate concretion related with methanogenesis arising from bacterial activities in the fermentation zone have $\delta^{13}C$ values ranged from 10.0‰ to 14.2‰ [47]. Furthermore, the release of CH_4 may also promote the prosperity of methanotroph with biomarkers of ^{13}C-depleted 3β-methylhopanes [48]. Extended 3β-methylhopanes up to C_{45} identified from the sediments of K_2qn^1 in the Songliao Basin support robust methanogenesis during the early diagenetic stage [49]. Highly depleted $\delta^{13}C_{org}$ values (minimum −32.4‰) and increased C/N values (maximum 25.6) of K_2qn^1 were interpreted as influences from methanogenesis and methanotroph [35]. The $\delta^{13}C$ values of ankerite associated with high content chlorite are from 1.9‰ to 3.0‰, slightly lower than the more aggregated ankerite but still heavier than those of the ostracod shells (Figure 7). Differences of the $\delta^{13}C$ values of ankerites from these two types of ostracods might be from the degree of shell closure and the proportion of clays entering into. The precipitation of chlorite prior to ankerite was another important factor, resulting in slightly weaker methanogenesis, and Fe^{2+} generated through DIR were bound within chlorite.

Therefore, the identified early diagenesis of two types of ostracods recorded in our study involved DIR, BSR, and methanogenesis through the production of Fe^{2+}, H_2S, CH_4 and HCO_3^- (Figure 8). Although chlorite, pyrite, and ankerite in these ostracods were formed in the ferric reduction zone, sulfate reduction zone, and methanogenic zone, respectively, low abundance of sulfate makes the other two redox processes more important. High amounts of ankerite with slightly heavier $\delta^{13}C$ values and low contents of pyrite also suggest a ferric-methane transition zone (FMTZ) without a sulfate reduction zone between them (Figure 8). This transition zone might be of great importance in the sulfate-poor and ferruginous water dominated Precambrian ocean [50] and might induce methane release to maintain long-term warm-house [51]. This also can be used to explain the massive ^{13}C-enriched carbonate rock deposits in Precambrian without large-scale black shale deposits [52,53]. However, it should be noted that the ankerite found in ostracods might be different from the dolomite nodules and layers found in the K_2qn^1, which were formed in a dynamically varied diagenetic water redox conditions [21]. The dolomite nodule was suggested to have a primary form as dolomite and a gradual transformation into ankerite as well as manganese-ankerite [21]. Rare earth elements and Sr isotope values also provide further evidence for the formation of dolomite nodules and layers resulting from the seawater intrusion events of the Songliao Basin [53,54].

4.2. Implications for the Geochemical Analyses of Ostracod

In situ $\delta^{13}C$ analysis revealed obvious differences between calcified shells and filled early diagenetic ankerites of ostracods (Figure 7), indicating certain interferences from secondary minerals on the primary DIC signals recorded in the calcified shells. In fact, before conducting the geochemical analysis with ostracod fossils, fine treatment is necessary, such as the visual examination for possible secondary carbonate minerals and the following brushing [17] and roasting for a certain time at high temperature in vacuum to remove organic matter [55]. However, some uncertainties still exist from extraneous aspects, such as the selection of cleaning methods, specimen ontogenetic stage, and shell preservation. Based on cleaning tests, clay minerals adhering to the shells have been considered as major contaminants in specimens [56]. Although the diagenetic dolomite and ankerite wrapped in ostracod are difficult to find and remove, they should be considered another noteworthy contaminant. Thus, we suggest to use strict treatment and high-resolution analysis to improve the reliability of ostracod-based geochemical data. Furthermore, detailed works are necessary to obtain a high-resolution $\delta^{13}C_{DIC}$ curve of the paleo-Songliao lake if we want to better understand the carbon cycle model in the Songliao Basin between oceanic anoxic event 2 (OAE2) and OAE3 [35].

5. Conclusions

Diagenesis keeps us in doubt about the representativeness of many geochemical indicators, especially the isotope and mineral related, forcing us to choose the carrier that formed in the water column and remained stable during diagenesis. Ostracoda are a good geochemical carrier of paleo-water and paleo-climate information and are widely used in the paleo-environment reconstruction. We identified DIR, BSR, and methanogenesis in the ostracods during their burial in the Songliao Basin 91.35 Ma. For the scarcity of sulfate in the pore water, a ferric-methane transition zone is suggested to control the formation of ^{13}C-enriched authigenic ankerite, which may be of great importance in the sulfate-poor but ferruginous water dominated Precambrian ocean. We also suggested strict treatment and high-resolution analysis to improve the reliability of ostracod-based geochemical data.

Author Contributions: Conceptualization, Z.L. and H.W. (Huajian Wang); methodology, Z.L., Y.L. and H.W. (Huajian Wang); investigation, Z.L., Y.L., D.L. and H.W. (Huajian Wang); resources, H.W. (Huajian Wang) and H.W. (Huaichun Wu); data curation, Z.L., Y.L. and X.D.; writing—original draft preparation, Z.L. and Y.L.; writing—review and editing, Z.L., Y.L., X.D. and H.W. (Huajian Wang);

supervision, H.W. (Huaichun Wu) and H.W. (Huajian Wang); project administration, H.W. (Huaichun Wu) and H.W. (Huajian Wang); funding acquisition, H.W. (Huajian Wang) and H.W. (Huaichun Wu). All authors have read and agreed to the published version of the manuscript.

Funding: This research was funded by the National Key R&D Program of China (grant no. 2019YFC0 605403), the National Natural Science Foundation of China (grant no. 41872125, 42002158, 41790451) and the scientific and technological projects of RIPED (grant no. 2021ycq01, yjkt2019-3).

Acknowledgments: We thank Wang Yongsheng for his help on the LA-IRMS analysis.

Conflicts of Interest: The authors declare no conflict of interest.

References

1. Derry, L.A. A burial diagenesis origin for the Ediacaran Shuram–Wonoka carbon isotope anomaly. *Earth Planet. Sci. Lett.* **2010**, *294*, 152–162. [CrossRef]
2. Shields, G.; Stille, P. Diagenetic constraints on the use of cerium anomalies as palaeoseawater redox proxies: An isotopic and REE study of Cambrian phosphorites. *Chem. Geol.* **2001**, *175*, 29–48. [CrossRef]
3. Phan, T.T.; Hakala, J.A.; Lopano, C.L.; Sharma, S. Rare earth elements and radiogenic strontium isotopes in carbonate minerals reveal diagenetic influence in shales and limestones in the Appalachian Basin. *Chem. Geol.* **2019**, *509*, 194–212. [CrossRef]
4. Maloof, A.C.; Rose, C.V.; Beach, R.; Samuels, B.M.; Calmet, C.C.; Erwin, D.H.; Poirier, G.R.; Yao, N.; Simons, F.J. Possible animal-body fossils in pre-Marinoan limestones from South Australia. *Nat. Geosci.* **2010**, *3*, 653–659. [CrossRef]
5. Holmes, J.A.; Chivas, A.R. Ostracod shell chemistry—Overview. In *The Ostracoda: Applications in Quaternary Research*; American Geophysical Union: Washington, DC, USA, 2002; pp. 185–204.
6. Katz, M.E.; Cramer, B.S.; Franzese, A.; Hönisch, B.; Miller, K.G.; Rosenthal, Y.; Wright, J.D. Traditional and emerging geochemical proxies in foraminifera. *J. Foramin. Res.* **2010**, *40*, 165–192. [CrossRef]
7. Doney, S.C.; Fabry, V.J.; Feely, R.A.; Kleypas, J.A. Ocean acidification: The other CO_2 problem. *Annu. Rev. Mar. Sci.* **2009**, *1*, 169–192. [CrossRef]
8. Spero, H.J.; Lerche, I.; Williams, D.F. Opening the carbon isotope "vital effect" black box, 2, Quantitative model for interpreting foraminiferal carbon isotope data. *Paleoceanography* **1991**, *6*, 639–655. [CrossRef]
9. Spero, H.; Williams, D. Opening the carbon isotope "vital effect" black box 1. Seasonal temperatures in the euphotic zone. *Paleoceanography* **1989**, *4*, 593–601. [CrossRef]
10. Farouk, S.; Faris, M.; Bazeen, Y.S.; Elamri, Z.; Ahmad, F. Upper Campanian-lower Maastrichtian integrated carbon isotope stratigraphy and calcareous microplankton biostratigraphy of North-central Tunisia. *Mar. Micropaleontol.* **2021**, *166*, 102003. [CrossRef]
11. Westerhold, T.; Röhl, U.; Donner, B.; Zachos, J.C. Global extent of early Eocene hyperthermal events: A new Pacific benthic foraminiferal isotope record from Shatsky Rise (ODP Site 1209). *Paleoceanogr. Paleoclimatol.* **2018**, *33*, 626–642. [CrossRef]
12. Rodriguez-Lazaro, J.; Ruiz-Muñoz, F. A general introduction to ostracods: Morphology, distribution, fossil record and applications. In *Developments in Quaternary Sciences*; Elsevier: Amsterdam, The Netherlands, 2012; pp. 1–14.
13. Salas, M.J.; Vannier, J.; Williams, M. Early Ordovician ostracods from Argentina: Their bearing on the origin of binodicope and palaeocope clades. *J. Paleontol.* **2007**, *81*, 1384–1395. [CrossRef]
14. Regier, J.C.; Shultz, J.W.; Kambic, R.E. Pancrustacean phylogeny: Hexapods are terrestrial crustaceans and maxillopods are not monophyletic. *Proc. R. Soc. B* **2005**, *272*, 395–401. [CrossRef]
15. Benson, R.H. Ecology of ostracode assemblages. In *Treatise on Invertebrate Paleontology: Part Q. Arthropoda 3-Crustacea/Ostracoda*; Geological Society of American: McLean County, IL, USA, 1961; pp. 56–63.
16. Decrouy, L.; Vennemann, T.W.; Ariztegui, D. Controls on ostracod valve geochemistry: Part 2. Carbon and oxygen isotope compositions. *Geochim. Cosmochim. Acta* **2011**, *75*, 7380–7399. [CrossRef]
17. Chamberlain, P.; Wan, X.; Graham, S.A.; Carroll, A.R.; Doebbert, A.C.; Sageman, B.B.; Blisniuk, P.; Corson, K.; Zhou, W.; Wang, C. Stable isotopic evidence for climate and basin evolution of the Late Cretaceous Songliao basin, China. *Palaeogeogr. Palaeocl. Palaeocl.* **2013**, *385*, 106–124. [CrossRef]
18. Sun, F.; Hu, W.; Wang, X.; Cao, J.; Fu, B.; Wu, H.; Yang, S. Methanogen microfossils and methanogenesis in Permian lake deposits. *Geology* **2021**, *49*, 13–18. [CrossRef]
19. Wang, H.; Ye, Y.; Deng, Y.; Liu, Y.; Lyu, Y.; Zhang, F.; Wang, X.; Zhang, S. Multi-element imaging of a 1.4 Ga authigenic siderite crystal. *Minerals* **2021**, *11*, 1395. [CrossRef]
20. Khan, D.; Qiu, L.; Liang, C.; Martizzi, P.; Mirza, K.; Liu, J. Tracing forming mechanism of the sparry calcite growth in the lacustrine shale of east China: A glimpse into the role of organic matter in calcite transformation. *Geol. J.* **2022**, *57*, 1820–1836. [CrossRef]
21. Liu, Y.; He, W.; Zhang, J.; Liu, Z.; Chen, F.; Wang, H.; Ye, Y.; Lyu, Y.; Gao, Z.; Yu, Z.; et al. Multi-element Imaging Reveals the Diagenetic Features and Varied Water Redox Conditions of a Lacustrine Dolomite Nodule. *Geofluids* **2022**, *2022*, 9019061.
22. Wang, H.J.; Ye, Y.T.; Deng, Y.; Wang, X.M.; Hammarlund, E.U.; Fan, H.F.; Canfield, D.E.; Zhang, S.C. Isotope evidence for the coupled iron and carbon cycles 1.4 billion years ago. *Geochem. Perspect. Lett.* **2022**, *21*, 1–6. [CrossRef]

23. Wang, T.T.; Ramezani, J.; Wang, C.S.; Wu, H.C.; He, H.Y.; Bowring, S.A. High-precision U–Pb geochronologic constraints on the Late Cretaceous terrestrial cyclostratigraphy and geomagnetic polarity from the Songliao Basin, Northeast China. *Earth Planet. Sci. Lett.* **2016**, *446*, 37–44. [CrossRef]
24. Wu, H.; Zhang, S.; Jiang, G.; Hinnov, L.; Yang, T.; Li, H.; Wan, X.; Wang, C. Astrochronology of the Early Turonian–Early Campanian terrestrial succession in the Songliao Basin, northeastern China and its implication for long-period behavior of the Solar System. *Palaeogeogr. Palaeocl. Palaeocl.* **2013**, *385*, 55–70. [CrossRef]
25. Wu, H.; Hinnov, L.A.; Zhang, S.; Jiang, G.; Yang, T.; Li, H.; Xi, D.; Ma, X.; Wang, C. Continental geological evidence for Solar System chaotic behavior in the Late Cretaceous. *GSA Bull.* 2022, *in press*. [CrossRef]
26. Feng, Z.Q.; Jia, C.Z.; Xie, X.N.; Zhang, S.; Feng, Z.H.; Cross, T.A. Tectonostratigraphic units and stratigraphic sequences of the nonmarine Songliao basin, northeast China. *Basin Res.* **2010**, *22*, 79–95.
27. Feng, Z.; Fang, W.; Li, Z.; Wang, X.; Huo, Q.; Huang, C.; Zhang, J.; Zeng, H. Depositional environment of terrestrial petroleum source rocks and geochemical indicators in the Songliao Basin. *Sci. China Earth Sci.* **2011**, *54*, 1304–1317. [CrossRef]
28. Wang, C.; Scott, R.W.; Wan, X.; Graham, S.A.; Huang, Y.; Wang, P.; Wu, H.; Dean, W.E.; Zhang, L. Late Cretaceous climate changes recorded in Eastern Asian lacustrine deposits and North American Epieric sea strata. *Earth Sci. Rev.* **2013**, *126*, 275–299. [CrossRef]
29. Wan, X.; Zhao, J.; Scott, R.W.; Wang, P.; Feng, Z.; Huang, Q.; Xi, D. Late Cretaceous stratigraphy, Songliao Basin, NE China: SK1 cores. *Palaeogeogr. Palaeocl. Palaeocl.* **2013**, *385*, 31–43. [CrossRef]
30. Sharp, Z.; Cerling, T. A laser GC-IRMS technique for in situ stable isotope analyses of carbonates and phosphates. *Geochim. Cosmochim. Acta* **1996**, *60*, 2909–2916. [CrossRef]
31. Pan, S.; Liang, S.; Ma, L.; Liu, C.; Liu, H. Genesis, distribution, and hydrocarbon implications of ostracod-bearing beds in the Songliao Basin (NE China). *Aust. J. Earth Sci.* **2017**, *64*, 793–806. [CrossRef]
32. Canfield, D.E. Reactive iron in marine sediments. *Geochim. Cosmochim. Acta* **1989**, *53*, 619–632. [CrossRef]
33. Slaughter, M.; Hill, R.J. The influence of organic matter in organogenic dolomitization. *J. Sediment. Res.* **1991**, *61*, 296–303. [CrossRef]
34. Wang, P.; Huang, Y.; Wang, C.; Feng, Z.; Huang, Q. Pyrite morphology in the first member of the Late Cretaceous Qingshankou formation, Songliao Basin, northeast China. *Palaeogeogr. Palaeocl. Palaeocl.* **2013**, *385*, 125–136. [CrossRef]
35. Jones, M.M.; Ibarra, D.E.; Gao, Y.; Sageman, B.B.; Selby, D.; Chamberlain, C.P.; Graham, S.A. Evaluating Late Cretaceous OAEs and the influence of marine incursions on organic carbon burial in an expansive East Asian paleo-lake. *Earth Planet. Sci. Lett.* **2018**, *484*, 41–52. [CrossRef]
36. Hardie, L.A. Dolomitization; a critical view of some current views. *J. Sediment. Res.* **1987**, *57*, 166–183. [CrossRef]
37. Bekker, A.; Slack, J.F.; Planavsky, N.; Krapež, B.; Hofmann, A.; Konhauser, K.O.; Rouxel, O.J. Iron formation: The sedimentary product of a complex interplay among mantle, tectonic, oceanic, and biospheric processes. *Econ. Geol.* **2010**, *105*, 467–508. [CrossRef]
38. Sánchez-Román, M.; Vasconcelos, C.; Schmid, T.; Dittrich, M.; McKenzie, J.A.; Zenobi, R.; Rivadeneyra, M.A. Aerobic microbial dolomite at the nanometer scale: Implications for the geologic record. *Geology* **2008**, *36*, 879–882. [CrossRef]
39. Vasconcelos, C.; McKenzie, J.A.; Bernasconi, S.; Grujic, D.; Tiens, A.J. Microbial mediation as a possible mechanism for natural dolomite formation at low temperatures. *Nature* **1995**, *377*, 220–222. [CrossRef]
40. Gregg, J.M.; Bish, D.L.; Kaczmarek, S.E.; Machel, H.G. Mineralogy, nucleation and growth of dolomite in the laboratory and sedimentary environment: A review. *Sedimentology* **2015**, *62*, 1749–1769. [CrossRef]
41. Matsumoto, R.; Iijima, A. Origin and diagenetic evolution of Ca–Mg–Fe carbonates in some coalfields of Japan. *Sedimentology* **1981**, *28*, 239–259. [CrossRef]
42. Canfield, D.E.; Raiswell, R. Pyrite formation and fossil preservation. In *Taphonomy: Releasing the Data Locked in the Fossil Record*; Plenum Press: New York, NY, USA, 1991; pp. 337–387.
43. Canfield, D.E.; Zhang, S.C.; Wang, H.J.; Wang, X.M.; Zhao, W.Z.; Su, J.; Bjerrum, C.; Haxen, E.; Hammarlund, E. A Mesoproterozoic Iron Formation. *Proc. Nat. Acad. Sci. USA* **2018**, *115*, E3895–E3904. [CrossRef]
44. Jiang, G.; Shi, X.; Zhang, S.; Wang, Y.; Xiao, S. Stratigraphy and paleogeography of the Ediacaran Doushantuo Formation (ca. 635–551Ma) in South China. *Gondwana Res.* **2011**, *19*, 831–849. [CrossRef]
45. Canfield, D.E.; Thamdrup, B. Towards a consistent classification scheme for geochemical environments, or, why we wish the term 'suboxic' would go away. *Geobiology* **2009**, *7*, 385–392. [CrossRef] [PubMed]
46. Summons, R.E.; Franzmann, P.D.; Nichols, P.D. Carbon isotopic fractionation associated with methylotrophic methanogenesis. *Org. Geochem.* **1998**, *28*, 465–475. [CrossRef]
47. Zhu, R.; Cui, J.; Luo, Z.; Li, S.; Mao, Z.; Xi, K.; Su, L. Isotopic geochemical characteristics of two types of carbonate concretions of Chang 7 member in the middle-upper Triassic Yanchang Formation, Ordos Basin, Central China. *Mar. Petrol. Geol.* **2020**, *116*, 104312. [CrossRef]
48. Summons, R.E.; Jahnke, L.L.; Roksandic, Z. Carbon isotopic fractionation in lipids from methanotrophic bacteria: Relevance for interpretation of the geochemical record of biomarkers. *Geochim. Cosmochim. Acta* **1994**, *58*, 2853–2863. [CrossRef] [PubMed]
49. Zhu, C.; Cui, X.; He, Y.; Kong, L.; Sun, Y. Extended 3β-methylhopanes up to C_{45} in source rocks from the Upper Cretaceous Qingshankou Formation, Songliao Basin, northeast China. *Org. Geochem.* **2020**, *142*, 103998. [CrossRef]
50. Fakhraee, M.; Hancisse, O.; Canfield, D.E.; Crowe, S.A.; Katsev, S. Proterozoic seawater sulfate scarcity and the evolution of ocean–atmosphere chemistry. *Nat. Geosci.* **2019**, *12*, 375–381. [CrossRef]

51. Pavlov, A.A.; Hurtgen, M.T.; Kasting, J.F.; Arthur, M.A. Methane-rich Proterozoic atmosphere? *Geology* **2003**, *31*, 87–90. [CrossRef]
52. Cui, H.; Warren, L.V.; Uhlein, G.J.; Okubo, J.; Liu, X.-M.; Plummer, R.E.; Baele, J.-M.; Goderis, S.; Claeys, P.; Li, F. Global or regional? Constraining the origins of the middle Bambuí carbon cycle anomaly in Brazil. *Precambrian Res.* **2020**, *348*, 105861. [CrossRef]
53. Cadeau, P.; Jézéquel, D.; Leboulanger, C.; Fouilland, É.; Floc'h, L.; Chaduteau, C.; Milesi, V.; Guélard, J.; Sarazin, G.; Katz, A. Carbon isotope evidence for large methane emissions to the Proterozoic atmosphere. *Sci. Rep.* **2020**, *10*, 1–13. [CrossRef]
54. Liu, Y.; Wang, H.; Zhang, J.; Liu, Z.; Chen, F.; Wang, X.; Zhang, S.; Liu, H. Rare earth elemental and Sr isotopic evidence for seawater intrusion event of the Songliao Basin 91 million years ago. *Petrol. Sci.* 2022, *in press*. [CrossRef]
55. Schwalb, A.; Lister, G.S.; Kelts, K. Ostracode carbonate δ18O-and δ13C-signature of hydrological and climatic changes affecting Lake Neuchâtel, Switzerland, since the latest Pleistocene. *J. Paleolimnol.* **1994**, *11*, 3–17. [CrossRef]
56. Rodríguez, M.; De Baere, B.; François, R.; Hong, Y.; Yasuhara, M.; Not, C. An evaluation of cleaning methods, preservation and specimen stages on trace elements in modern shallow marine ostracod shells of Sinocytheridea impressa and their implications as proxies. *Chem. Geol.* **2021**, *579*, 120316. [CrossRef]